# INSTITUTE FOR FUSION STUDIES

DOE/ET-53088-496 IFSR #496

Nonlinear Dynamics of the Relativistic Standard Map

Y. NOMURA, Y.H. ICHIKAWA, and W. HORTON
Institute for Fusion Studies
The University of Texas at Austin
Austin, Texas 78712

April 1991

# THE UNIVERSITY OF TEXAS

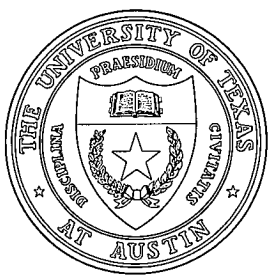


# AUSTIN

# Nonlinear Dynamics of the Relativistic Standard Map

Y. Nomura, Y.H. Ichikawa, and W. Horton
Institute for Fusion Studies
The University of Texas at Austin
Austin, Texas 78712

**Abstract**

Heating and acceleration of charged particles by RF fields have been extensively investigated by the standard map. The question arises as to how the relativistic effects change the nonlinear dynamical behavior described by the classical standard map. The relativistic standard map is a two parameter $(K, \beta = \omega/kc)$ family of dynamical systems reducing to the standard map when $\beta \to 0$. For $\beta \neq 0$ the relativistic mass increase suppresses the onset of stochasticity. It is shown that the speed of light limits the rate of advance of the phase in the relativistic standard map and introduces KAM surfaces persisting in the high momentum region. An intricate structure of mixing in the higher order periodic orbits and chaotic orbits is analyzed using the symmetry properties of the relativistic standard map. The interchange of the stability of the periodic orbits in the relativistic standard map is also observed and is explained by the local linear stability of the orbits.

# I. Introduction

Understanding of the stability of the nonlinear motion of charged particles in confining and accelerating electromagnetic fields has been advanced by studies of the standard map. The standard map,[1] with its single parameter $K$, applies to a wide class of problems including the confinement of particles in magnetic fusion devices,[2-3] the radio frequency heating of particles[4] and the Newtonian acceleration of particle by an infinite sequence of longitudinal plasma waves with equal amplitudes and evenly spaced phase velocities. Thus, it is natural to pose the question how relativistic effects change the nonlinear motion described by the classical standard map.

Several years ago, Tajima and Dawson[5] proposed the plasma-laser electron accelerator based on the injection of an electromagnetic wave packet of high power radiation into an underdense plasma which produces an electrostatic accelerating wake field excited behind the photon beam. This plasma beat-wave acceleration concept has been pursued intensively from a theoretical viewpoint, as well as with simulation and experimental studies.[6] Due to the interest of exploring such new acceleration mechanisms, we have undertaken a systematic study of the nonlinear dynamics of the relativistic standard map. Recently, Chernikov *et al.*[7] have independently introduced the relativistic map and studied how the properties of particle acceleration and the deterministic diffusion are modified by the relativistic generalization of the standard map.

Extending our studies of the classical standard map,[8] we report a systematic study of the nonlinear dynamics of the relativistic standard map. According to the terminology of two-dimensional mappings, the classical (Newtonian) standard map is identified as a radial twist map with a linear phase advancement. The relativistic effect from the Lorentz acceleration equation takes into account the finite speed of light by introducing the additional parameter $\beta(=\omega/kc)$. The parameter $\beta$ controls the strength of the nonlinearity in the phase advance

equation for the map. The nonlinearity of the phase advance in the relativistic regime makes the long-time dynamics fundamentally different from that in the Newtonian map.

We describe the fundamental properties of the two parameter $(K, \beta)$ relativistic standard map in Sec. II, and we illustrate characteristic motions of particles in the phase space in Sec. III. We show that there is the persistence of multi-periodic regular motions as high as the period-54 orbits in the ultra-relativistic case of $\beta = 10\pi$ for $K = 1.30$. The intricate structure of the periodic orbits is best analyzed by the symmetry properties of the relativistic standard map in Sec. IV. We observe also the interchange in the positions of the stable islands and unstable islands with the change of the parameter $\beta$. The details of the analysis of this phenomena are discussed in Sec. V. In Sec. VI we analyze the Poincaré-Birkhoff multifurcation around the fundamental period-4 orbit. In Sec. VII, we give the concluding remarks.

# II. Fundamental Properties of the Relativistic Standard Map

Let us consider an electrostatic wave packet, having the constant amplitude $E_0$, a given wavenumber $k$ and an infinite spectrum of harmonic frequencies with separation $\omega$, given as

$$E(x,t) = E_0 \sum_{n=-\infty}^{\infty} \sin(kx - n\omega t) \ . \tag{1}$$

Relativistic motion of an electron, having the rest mass $m_0$, charge $-e$, in the above electric field is determined by the Hamiltonian

$$H = \sqrt{p^2c^2 + m_0^2c^4} - e\phi(x,t) \ , \tag{2}$$

$$\phi = \frac{E_0}{k} \sum_{n=-\infty}^{\infty} \cos(kx - n\omega t) \ , \tag{3}$$

where $c$ is the light speed and $p$ is the relativistic momentum $m_0\gamma v$. The equation of motion of the electron is

$$\frac{dx}{dt} = \frac{\partial H}{\partial p} = \frac{pc^2}{(m_0^2c^4 + p^2c^2)^{1/2}} \tag{4}$$

$$\frac{dp}{dt} = -\frac{\partial H}{\partial x} = -eE_0 \sum_{n=-\infty}^{\infty} \sin(kx - n\omega t)$$

$$= -\frac{2\pi}{\omega} eE_0 \sin(kx) \sum_{n=-\infty}^{\infty} \delta\left(t - \frac{2n\pi}{\omega}\right) , \tag{5}$$

where $\delta(z)$ is the Dirac delta function. It is appropriate to normalize the variables $x, p$ and $t$ as the non-dimensional quantities $X, P, T$ defined by

$$X \equiv \frac{k}{2\pi} x , \quad P \equiv \frac{k}{m_0\omega} p , \quad T \equiv \omega t . \tag{6}$$

The 1-$\frac{1}{2}$ D Hamiltonian motion from Eqs. (4) and (5) reduces to the analytic description of the surface of section mapping in the $(X, P)$ plane obtained by integrating through the impulses given in Eq. (5). The corresponding Poincaré mapping at times $T_n = 2n\pi$ is written down immediately as

$$P_{n+1} = P_n + F(X_n) \tag{7}$$

$$X_{n+1} = X_n + G(P_{n+1}) \tag{8}$$

with the definitions of

$$F(X) = -\frac{K}{2\pi} \sin(2\pi X) \tag{9}$$

$$G(P) = \frac{P}{\sqrt{1 + \beta^2 P^2}} . \tag{10}$$

Here the parameters $K$ and $\beta$ are given by

$$K \equiv 4\pi^2 eE_0 k/m_0\omega^2 \quad \text{and} \quad \beta = \omega/kc , \tag{11}$$

respectively. The two-dimensional map defined by Eqs. (7)–(10) is the relativistic standard map which reduces to the classical (Newtonian) standard map in the limit of $\beta \to 0$.

It is straightforward to confirm that the relativistic map is area preserving, and that it is invariant under the translation $X \to X + 1$, but is not periodic with respect to the momentum $P$. Therefore, the relativistic standard map possesses only fixed points as its equilibrium points, and thus the well-known accelerator modes of the classical standard map do not exist in the relativistic standard map. The positions of the fixed points are determined for $m = 0, \pm 1, \pm 2, \ldots$ by

$$(X_m, P_m)_s = \left(0,\ m(1-\beta^2 m^2)^{-1/2}\right) \tag{12}$$

$$(X_m, P_m)_u = \left(1/2,\ m(1-\beta^2 m^2)^{-1/2}\right)\ . \tag{13}$$

Hence, we find that the fixed points exist with unequal intervals within the range determined by the limit $|m| < \beta^{-1}$. If $\beta > 1$, the only fixed points $(X, P)$ are $(0, 0)$ and $(1/2, 0)$. When $\beta = m^{-1}$, at the $m$-th fixed point $P_m$ becomes infinity, which is the resonance acceleration investigated by Chernikov *et al.*[7] They observed that a chaotic channel is opened at $X = \pm 1/2$ for $\beta = m^{-1}$, and along the chaotic channel particles can be accelerated to arbitrary high energies.

Now, the stability of the fixed points is determined from the residue $R$ of the tangent map

$$\begin{pmatrix} \Delta P_{n+1} \\ \Delta X_{n+1} \end{pmatrix} = \Delta T \begin{pmatrix} \Delta P_n \\ \Delta X_n \end{pmatrix} \tag{14}$$

where $\Delta T$ is the tangent map

$$\Delta T = \begin{pmatrix} 1 & F'(X_n) \\ G'(P_n) & 1 + F'(X_n)G'(P_n) \end{pmatrix} \tag{15}$$

associated with the relativistic standard map (7)–(10). The residue $R$ is given as

$$R \equiv \frac{1}{2} - \frac{1}{4} Tr(\Delta T) = -\frac{1}{4} F'(X_n)G'(P_n)\ . \tag{16}$$

The fixed point is stable if $0 < R < 1$, which gives rise to

$$0 < K\cos(2\pi X_m) < 4(1-\beta^2 m^2)^{-3/2} \ . \tag{17}$$

Therefore, we find that as far as $K > 0$, the fixed point $(X_m, P_m)_u$ given by Eq. (13) remains unstable, while the fixed point $(X_m, P_m)_s$ is stable for $K$ in the range

$$0 < K < 4(1-\beta^2 m^2)^{-3/2} \tag{18}$$

For the stable orbits the average rotation number $\rho$ is given by

$$\rho \equiv \frac{1}{2\pi}\cos^{-1}(1-2R) \ . \tag{19}$$

If the rotation number $\rho$ becomes equal to $p/q$ ($p$ and $q$ are primes), the Poincaré-Birkhoff period-$q$ islands bifurcate out of the fixed point $(X_m, P_m)_s$. The onset of the period-$q$ bifurcation takes place as $K$ passes through the value

$$K(p/q) = 2(1-\beta^2\, m^2)^{-3/2}\left[1-\cos\left(2\pi\,\frac{p}{q}\right)\right] \ . \tag{20}$$

It is worthwhile to remark that at the $m = 0$ fixed point, i.e. the origin $(0,0)$, the onset condition of (20) becomes identical with that of the classical standard map. Hence, the structure of the orbits around the origin is expected to be similar to that of the classical standard map.

# III. Regular Motion of Particles

In order to investigate the characteristic features of the dynamics determined by the relativistic standard map, let us begin our analysis with the results of the numerical observations of the particle motions in the phase space. Since it is known that the classical standard map ($\beta = 0$) exhibits the global stochasticity above the threshold value of $K_c = 0.97$, we choose the nonlinear parameter $K = 1.30$, where the regular motion prevails over the chaotic motion in the classical standard map. Equation (20) with $\beta = 0$ tells us that for $K = 1.30$

the period-6 and higher periodic Poincaré-Birkhoff islands bifurcate at the origin, but the period-5 P-B islands are not yet borne out there.

In Fig. 1(a)–(d), we show traces for 5000 iterations of the orbits of 50 particles, which are initially distributed uniformly over the range of $-0.5 < x \leq +0.5$ with $P = 0$. Increasing the value of $\beta$, we observe that the relativistic effect suppresses the deterministic diffusion drastically. In particular, we notice that at $\beta = 0.1\pi$, the KAM surface is formed between the $m = 2$ fixed point island and the $m = 1$ island, even though Eq. (12) allows the stable $m = 3$ and $m = 2$ fixed points. At the value of $\beta = 0.2\pi$, the KAM surface is squeezed down to the place between the $m = 2$ island and the $m = 1$ island.

Now, increasing the value of $\beta$ above unity as shown in Fig. 2(a)–(d), we observe that when the relativistic effect dominates, the map exhibits a qualitatively different particle dynamics. At the larger value of $\beta$, the outermost KAM surface expands into the higher momentum region and coherent island structures prevail inside the region. In particular, we are astonished to count the period-20 islands in Fig. 2(c) for $\beta = 4\pi$, and as high as the period-54 in Fig. 2(d) for $\beta = 10\pi$.

Now we develop an analytic approximation for the observed phase space structure. Firstly, we give the shape of the outermost KAM surface by assuming $|X_{n+1} - X_n| \ll X_n$ and $|P_{n+1} - P_n| \ll P_n$ for large $n$. Equations (7) and (8) can be reduced to

$$\frac{dP}{dX} = \frac{F(X)}{G(P)} \tag{21}$$

which yields

$$\sqrt{1 + \beta^2 P^2} - \frac{K}{4\pi^2}\beta^2 \cos(2\pi X) = \text{const.} \tag{22}$$

Thus, for the initial condition of Fig. 2 given as $(X_0, P_0) = (1/2, 0)$, we get

$$P(X) = \frac{1}{\pi}\left[K\cos^2(\pi X) + \frac{K^2\beta^2}{4\pi^2}\cos^4(\pi X)\right]^{1/2} . \tag{23}$$

The maximum attainable momentum $P_{\max}$ is estimated by the condition $dP/dX = 0$ as

$$P_{\max} = \frac{1}{\pi}\left(K + \frac{K^2}{4\pi^2}\beta^2\right)^{1/2} . \tag{24}$$

We confirmed that Eqs. (23) and (24) are in good agreement with the observed results given in Fig. 2.

Next, we turn to the periodic islands. According to Eq. (20), we expect to have the period-6 islands around the origin for $K = 1.3$. In the high momentum region far out from the origin, however, we notice that the phase advancement for one step of the iteration of map is approximately

$$\Delta X \simeq \frac{1}{\beta}\left(1 - \frac{1}{2}(\beta P)^{-3} + \cdots\right) . \tag{25}$$

Hence, the maximum periodicity $N$ will be determined by the condition

$$N\,\Delta X \simeq 2 , \tag{26}$$

which gives $N \approx 2\beta$, namely $N = 24$ for $\beta = 4\pi$ and $N = 62$ for $\beta = 10\pi$. These maximum periodicity numbers are consistent with the observation.

Lastly, we show in Fig. 3 the details of the islands structure for the values of $\beta = 0$, $\beta = 0.2\pi$ and $\beta = 4\pi$. Here, unlike Fig. 1 and Fig. 2, we put the particles at the places where the periodic islands exist. As for Fig. 3(a) and (b), we set the particles along the $X$-axis and also along the curves of $X = G(P)$ over the range of $0 < P < 1.0$. While for Fig. 3(c), the particles are distributed only along the curve of $2X = G(P)$ over the range of $0 < P < 1.0$, resulting in the empty period-8 islands around the origin. Fig. 3(b) shows that the $m = 1$ fixed point is indeed stable, though it cannot be reached from the initial positions of $P = 0$. Furthermore, we call attention to the fact that the period-8 islands are stable on the $X$-axis ($P = 0$) at the value of $\beta = 0.2\pi$, while for the larger value of $\beta = 4\pi$, the period-8 orbits on the $X$-axis ($P = 0$) turn out to be unstable. This interchange of stable and unstable orbits in the phase space is analyzed in Sec. V.

# IV. Symmetries of the Relativistic Standard Map

Although we have given a reliable estimate in Eqs. (25)–(26) for the multiplicity of the periodic orbits in terms of the constant phase advancement in the ultra-relativistic case, we wish to develop a theory for the overall structure of the regular motion of particles in the relativistic standard map. For this purpose, the analysis of the symmetries of the mappings provides the key instrument. Greene *et al.*[9] have discussed the global behavior of the area-preserving map on the basis of the symmetries. Pina and Lara[10] carried out an explicit analysis of the symmetries of the classical standard map. Introducing the symmetries with respect to the space inversion and to the momentum inversion, Ichikawa *et al.*[11] developed extensive analysis of the regular motion of the classical standard map.

A map is called reversible if there exists an involution $I_0$ which satisfies the relation

$$T \cdot I_0 \cdot T = I_0 \qquad \text{and} \qquad I_0 \cdot I_0 = I_d \tag{27}$$

where $I_d$ stands for the unity matrix. This relation indicates that the reversible map can be expressed as the product of two involutions

$$T = I_1 \cdot I_0 \ , \qquad I_1 \cdot I_1 = I_d \tag{28}$$

with the definition of

$$I_1 = T \cdot I_0 \tag{29}$$

and the inverse transformation $T^{-1}$ is given by

$$T^{-1} = I_0 \cdot I_1 \ . \tag{30}$$

If we define $I_j$ as the $j$-th iteration of the map $T$ on the involution $I_0$, $I_j = T^j \cdot I_0$, and confirm that $I_j$ is also an involution. The ensemble of $I_j$ and $T^k$ for arbitrary integers $j$ and $k$ forms a discrete infinite group with the relationships

$$I_j \cdot I_k = T^{j-k} \ , \qquad T^j \cdot I_k = I_{j+k} \ , \qquad I_j \cdot T^k = T^{j-k} \ . \tag{31}$$

It can be shown that the fixed points of the involution $I_j$ form a curve $\Gamma_j$ which is known as its symmetry line:

$$\Gamma_j: \qquad \left\{ \mathbb{R} \middle| I_j \cdot \mathbb{R} = \mathbb{R} \right\} . \tag{32}$$

Therefore, the first equation of (31) states that the intersection of $\Gamma_j$ and $\Gamma_k$ determine the periodic points of $T$, of which period $N$ divides $|j-k|$. From the second and the third relations of Eq. (31), we can deduce that the symmetry lines $\Gamma_j$ are transformed by $T^n$ into other symmetry lines according to the relation

$$\Gamma_{2N+j} = T^N \Gamma_j \ , \tag{33}$$

which enables us to construct the family of symmetry lines of arbitrary order.

For a generic form of the two-dimensional map as given in Eqs. (7)–(10), if the transformation function of $F(X)$ is antisymmetric with respect to space inversion, $F(-X) = -F(X)$, the map is expressible as the composition of the following two involutions:

$$\begin{aligned} I_0: &\quad P' = P + F(X) \ , &\quad X' &= -X \\ I_1: &\quad P' = P \ , &\quad X' &= -X + G(P) \end{aligned} \tag{34}$$

The symmetry lines of these two fundamental involutions are given by

$$\Gamma_0: \qquad X = 0 \qquad \Gamma_1: \qquad 2X - G(P) = 0 \ . \tag{35}$$

Writing an expression for the symmetry line for $I_j$ symbolically as $\Gamma_j(\mathbb{R}) = 0$, we have

$$\begin{aligned} \Gamma_j(\mathbb{R}) &= \Gamma_{j-2}(T^{-1}\mathbb{R}) = 0 \\ \Gamma_j(\mathbb{R}) &= \Gamma_{j+2}(T\mathbb{R}) = 0 \end{aligned} \tag{36}$$

which provides us with the following recurrence formulas

$$\begin{aligned} \Gamma_j[X,P] &= \Gamma_{j-2}\left[X - G(P) \ , \ P - F\{X - G(P)\}\right] \\ \Gamma_j[X,P] &= \Gamma_{j+2}\left[X + G\{P + F(X)\} \ , P + F(X)\right] \ . \end{aligned} \tag{37}$$

Explicitly, we have

$$\Gamma_2: \qquad X - G(P) = 0$$

$$\Gamma_3: \quad 2X - 2G(P) - G\left[P - F\{X - G(P)\}\right] = 0 \tag{38}$$

$$\Gamma_4: \quad X - 2G(P) - G\left[P - F\{X - G(P)\}\right] = 0$$

and

$$\Gamma_{-1}: \quad 2X + G\left[P + F(X)\right] = 0$$

$$\Gamma_{-2}: \quad X + G\left[P + F(X)\right] = 0 \tag{39}$$

$$\Gamma_{-3}: \quad 2X + 2G\left[P + F(X)\right] + G\left[P + F(X) + F\{X + G(P + F(X)\}\right] = 0 \ .$$

In the previous section, we have made use of the $\Gamma_2$ symmetry line to construct Figs. 3(a) and (b), and the $\Gamma_1$ symmetry line to construct Fig. 3(c), so that we have been able to reproduce all aspects of the periodic island structure.

A factorization of the map into two involutions is not unique. Antisymmetry of the function $G(P)$ with respect to momentum inversion, $G(-P) = -G(P)$, gives rise to another involution decomposition $T = J_1 \cdot J_0$, with

$$J_0: \quad P' = -P \ , \ X' = X - G(P)$$

$$J_1: \quad P' = -P + F[X - G(P)] \tag{40}$$

$$X' = X - G(P) - G\left[P - F\{X - G(P)\}\right] \ .$$

This factorization defines the momentum inversion symmetry as

$$\begin{aligned} &\gamma_0: \quad P = 0 \\ &\gamma_1: \quad 2P - F[X - G(P)] = 0 \ . \end{aligned} \tag{41}$$

Since the same recurrence formula as Eqs. (37) are also valid for this momentum inversion symmetry, it is straightforward to write down the higher order symmetry lines as

$$\gamma_2: \quad P - F[X - G(P)] = 0$$

$$\gamma_3: \qquad 2P - 2F\,[X - G(P)] = 0 \tag{42}$$

$$\gamma_4: \qquad P - F[X - G(P)] - F[X - G(P) - G\{P - F(X - G(P))\}] = 0$$

and

$$\gamma_{-1}: \qquad 2P + F(X) = 0$$

$$\gamma_{-2}: \qquad P + F(X) = 0$$

$$\gamma_{-3}: \qquad 2P + 2F(X) + F\,[X + G\{P + F(X)\}] = 0\ . \tag{43}$$

Now, for the relativistic standard map, we show in Fig. 4 a family of the spatial inversion symmetry lines up to the 12-th order for the values of $K = 1.3$ and $\beta = 4\pi$. It is important to notice that in the region of $|P| \gtrsim \beta^{-1}$, the symmetry lines $\Gamma_j$ become parallel with the constant phase separation of $(2\beta)^{-1}$. Thus we confirm from the symmetry analysis that the phase increment at each step of the mapping is indeed given by $\beta^{-1}$ in accord with Eq. (25). Figure 5 illustrates a family of the momentum inversion symmetry lines up to the 12-th order. We observe that the higher order momentum inversion symmetry lines $\gamma_j$ approach asymptotically to the separatrix KAM surface. Thus, from the symmetry properties of the map, we are able to give a theoretical demonstration of the heuristic results given for the spacing of the islands and the limiting KAM surface given in Sec. III.

To conclude the present section we illustrate, with Figs. 6(a) and (b), the results of a superposition of Fig. 3(c) with Fig. 4 and Fig. 5, respectively. We can classify the even-number periodic islands into two groups, (i) $N = 2 \cdot (2\ell)$ and (ii) $N = 2 \cdot (2\ell + 1)$ with integers $\ell$. For the first group, intersections of the odd-number symmetry lines $\Gamma_{2j+1}$ determine the hyperbolic points and intersections of the even-number symmetry lines $\Gamma_{2j}$ determine the elliptic points. For the second group, intersections of the odd-number symmetry lines $\Gamma_{2j+1}$ determines the elliptic points and intersections of the even-number symmetry lines $\Gamma_{2j}$ determine

the hyperbolic points. As for the odd-number periodic islands, we remark that intersections of the symmetry lines $\Gamma_j$ determine only the unstable odd-periodic islands. Contrary to the spatial inversion symmetry, Fig. 5(b) shows that intersections of the odd-number symmetry lines $\gamma_{2j+1}$ determine all the elliptic even-periodic orbits, while intersections of the even-number symmetry lines $\gamma_{2j}$ determine all the hyperbolic even-periodic orbits. As for the odd-periodic islands, intersections of the symmetry lines $\gamma_j$ determine all the stable odd-periodic islands.

# V. Stability of the Periodic Orbits

At the end of Sec. III, we showed that the positions of the stable and unstable period-8 orbits are interchanged upon increasing the value of $\beta$. We have carried out an extensive survey of this interchange of the stability of periodic orbits with respect to variation of $\beta$ for several choices of the stochasticity parameter $K$. Figure 7 illustrates the features of this phenomena. Keeping our attention on the periodic orbits on the $X$-axis ($P = 0$), we see that the period-8 orbit with $X > 0$ is stable up to a $\beta$ value around $\beta \approx 2.5$, then it turns into unstable. At the same time the unstable period-6 orbit on the $X$-axis become stable. We also observe the occurrence of stable period-10 orbit. Increasing $\beta$ above 3.5, we see that these stable period-6 and 10 orbits are turning unstable while the period-8 hyperbolic point changes itself into the elliptic point. Figure 8(a) and (b) show such interchange of the stability of the period-3 and period-4 orbits at $K = 3.3$ for the values of $\beta = 2.20$ and $\beta = 2.83$. In particular, we notice that Fig. 8(b) indicates the appearance of two sets of period-3 orbits very close to the origin. Increasing the stochasticity parameter $K$ to 6.4717, we show similar phenomena in Figs. 9(a) and (b), where the stable fixed point at the origin has bifurcated into the period-2 orbit. We observe, however, the stability interchange of the period-3 and period-4 orbits takes place somewhere between $2.20 < \beta < 2.51$.

In order to investigate this interchange phenomena, we examine the local stability of

the periodic orbits in some detail. We aim to determine the critical values of $\beta$ where the stability interchange occurs. Since a period-$n$ orbit is a fixed point of the $T^n$ map, its local stability is determined by the eigenvalue of a matrix $L$ obtained by linearizing $T^n$ about one of its fixed points. The stability of the fixed point (or orbit) is determined by the residue $R$ at the fixed point, defined by

$$R \equiv \frac{1}{4}\left[2 - Tr(L)\right] . \tag{44}$$

The orbit is stable for $0 < R < 1$ and called elliptic. If $R < 0$, the orbit is directly unstable and called hyperbolic without reflection. For $R > 1$, the orbit is inversely unstable, called hyperbolic with reflection.

We find it is tractable to develop the stability analysis for the period-3 and period-4 orbits that multifurcate from the origin. For period-3 orbits, there are two groups of orbits. Location of these orbits is determined by the symmetry analysis discussed in the preceding section. Firstly, a periodic orbit with one point on the $X$-axis can be determined by the intersection of the momentum inversion symmetry lines, $\gamma_0$ and $\gamma_3$ (Eqs. (41) and (42):

$$P_0 = 0 , \quad 2F(X_0) + F\left[X_0 + G(F(X_0))\right] = 0 . \tag{45}$$

After a lengthy but straightforward calculation we find that the residue of this orbit is

$$R^{(3)}(X_0, P_0 = 0) = -\frac{1}{4}\left[2F'(X_0) + F'\left\{X_0 + G(F(X_0))\right\}\left\{1 + G'(F(X_0))F'(X_0)\right\}\right]$$

$$\times \left[2G'(F(X_0)) + G'(0)\left\{1 + G'(F(X_0))F'(X_0)\right\}\right] . \tag{46}$$

The other set of the period-3 orbits, with one point on the $P$-axis ($X_0 = 0$), is determined by the intersection of the space inversion symmetry lines, $\Gamma_0$ and $\Gamma_3$, from Eqs. (35) and (38),

$$X_0 = 0 , \qquad 2G(P_0) + G\left[P_0 + F(G(P_0))\right] = 0 . \tag{47}$$

For this orbit, the residue is calculated as

$$R^{(3)}(X_0 = 0, P_0) = -\frac{1}{4}\left[2G'(P_0) + G'\left\{P_0 + F(G(P_0))\right\}\left\{1 + F'(G(P_0))G'(P_0)\right\}\right]$$

$$\times \left[2F'(G(P_0)) + F'(0)\left\{1 + F'(G(P_0))G'(P_0)\right\}\right] \ . \tag{48}$$

Similarly, the location of the period-4 orbit, whose one point lies on the $X$-axis ($P = 0$), is specified by the intersection of the symmetry lines $\gamma_0$ and $\gamma_4$, from Eqs. (41) and (42))

$$P_0 = 0 \ , \qquad F[X_0 + F(X_0 + G(X_0)] = 0 \ . \tag{49}$$

For the transformation function of Eq. (9), Eq. (49) gives rise to the following two solutions:

$$\text{(a)} \qquad 2X_0^{(a)} + G(F(X_0^{(a)})) = 0 \ , \tag{50}$$

and

$$\text{(b)} \qquad G(F(X_0^{(b)})) = m + \frac{1}{2} \qquad (m\text{: integer}) \ . \tag{51}$$

When the nonlinear parameter $K$ satisfies the condition

$$K > 2 \ , \tag{52}$$

the $a$-branch period-4 orbits exist at $\left[X_0^{(a)}, P_0 = 0\right]$, $\left[-X_0^{(a)}, F(X_0^{(a)})\right]$, $\left[-X_0^{(a)}, P_0 = 0\right]$ and $\left[X_0^{(a)}, -F(X_0^{(a)})\right]$, which are mirror symmetric with respect to the origin. The residue of this period-4 orbit is calculated as

$$R^{(4)}(X_0^{(a)}, P_0 = 0) = -\frac{1}{4} F'(X_0^{(a)}) \left[2 + G'(F(X_0^{(a)}))\right] \left[2 + G'(0)F'(X_0^{(a)})\right]$$
$$\times \left[2G'(X_0^{(a)})) + G'(0)\left\{2 + G'(F(X_0^{(a)}))F'(X_0^{(a)})\right\}\right] \ . \tag{53}$$

Equation (51) gives rise to the $b$-branch period-4 orbits at the positions of $\left[X_0^{(b)}, P_0 = 0\right]$, $\left[X_0^{(b)} + 1/2, F(X_0^{(b)})\right]$, $\left[X_0^{(b)} + 1/2, P_0 = 0\right]$ and $\left[X_0^{(b)}, -F(X_0^{(b)})\right]$, provided that the nonlinear parameter $K$ satisfies the condition

$$K > 2\pi \cdot \left[(m + 1/2)^{-2} - \beta^2\right]^{-1/2} \ . \tag{54}$$

These orbits are mirror symmetric with respect to the point $\left(X_0^{(b)} + 1/4, P_0 = 0\right)$. Since the relativistic standard map is symmetric with respect to the origin, we have another set

of the $b$-branch period-4 orbits at the positions of $\left[-X_0^{(b)}, P_0 = 0\right]$, $\left[X_0^{(b)} - 1/2, F(+X_0^{(b)})\right]$, $\left[-X_0^{(b)} - 1/2, P_0 = 0\right]$ and $\left[-X_0^{(b)} + F(X_0^{(b)})\right]$, respectively. The residue of the pairs of these period-4 orbits is calculated as

$$R^{(4)}(X_0^{(b)}, P_0 = 0) = -\frac{1}{4} G'(F(X_0^{(b)})) F'(X_0^{(b)})^2 \times \left[G'(F(X_0^{(b)})) G'(0)^2 F'(X_0^{(b)})^2 - 4\left\{G'(0) + G'(F(X_0^{(b)}))\right\}\right] . \quad (55)$$

In addition to these sets of the period-4 orbit, we also have the period-4 orbit whose one point lies on the $P$-axis ($X = 0$). The location of this orbit is specified by the intersection of the space inversion symmetry lines, $\Gamma_0$ and $\Gamma_4$ (Eqs. (35) and (38))

$$X_0 = 0 , \quad G(P_0) + G\left[P_0 + F(G(P_0))\right] = 0 . \quad (56)$$

For the relativistic standard map with Eq. (9), Eq. (56) reduces to

$$2P_0 + F(G(P_0)) = 0 . \quad (57)$$

The residue of this orbit is calculated as

$$R^{(4)}(X_0 = 0, P_0) = -\frac{1}{4} G'(P_0) \left[2 + F'(G(P_0))\right] \left[2 + F'(0) G'(P_0)\right] \times \left[2F'(G(P_0)) + F'(0)\left\{2 + F'(G(P_0)) G'(P_0)\right\}\right] . \quad (58)$$

Having obtained analytic expressions for the residues of the period-3 orbits and the period-4 orbits, we can investigate the $\beta$-dependence of the residues by substituting values of the coordinates numerically determined for specified values of $\beta$. We show in Figs. 10 and 11 the $\beta$-dependence of the residue of the period-3 and the period-4 orbits at $K = 3.3$, respectively. We observe in Fig. 10 that the residues $R^{(3)}(X_0, P_0 = 0)$ and $R^{(3)}(X_0 = 0, P_0)$ of the period-3 orbits become zero at the value of $\beta = 2.40$, where the stability interchange takes place. As for the period-4 orbits, Fig. 11 indicates that all of them are unstable at

$\beta = 0$. As $\beta$ increases the $b$-branch turns stable and merges into the $a$-branch at $\beta = 0.612$. At the value of $\beta = 2.44$, the residues $R^{(4)}(X_0^{(a)}, P_0 = 0)$ and $R^{(4)}(X_0 = 0, P_0)$ of the period-4 orbits change their signs, leading to the interchange of their stability.

For the higher value of $K = 6.4717$, we show in Fig. 12 and 13 the $\beta$-dependence of the residue of the period-3 and the period-4 orbits. In contrast to the case of $K = 3.3$, the stable period-3 orbits survive only in a very narrow range of $\beta$. Consistent with the observed change in stability shown in Figs. 9(a) with $\beta = 2.20$ and (b) with $\beta = 2.51$, the stability interchange of the period-3 orbits takes place at $\beta = 2.34$. The residues of the period-4 orbits behave in a very complicated manner. At $\beta = 0$, every branch of the period-4 orbits are directly unstable. As $\beta$ increases, the $b$-branch undergoes rapid change from stable to inversely unstable and back to stable, then merging into the $a$-branch at $\beta = 1.749$. The residues $R^{(4)}(X_0^{(a)}, P_0 = 0)$ and $R^{(4)}(X_0 = 0, P_0)$ at $K = 6.4717$ change their signs at the value of $\beta = 2.28$, which confirms the stability interchange phenomena found numerically in Fig. 9(a) and (b). Here, we notice that the residue $R^{(4)}(X_0 = 0, P_0)$ is increasing from zero to unity and then falls below unity again. This peculiar variation of the residue of the period-4 orbits will be discussed further in the next section.

# VI. Poincaré-Birkhoff Multifurcation for the Period-4 Orbit

In the preceding section, we showed that the residue of the period-4 orbit increases to unity and then falls again as $\beta$ increases. We should be aware that stable orbits with the same value of residue but with different values of $\beta$ exhibit distinct behaviors. Referring to Figs. 11 and 13, we observe that for the same value of $R^{(4)} = 0$ the merging of the $b$-branch into the $a$-branch takes place at a smaller value of $\beta$, and the stability interchange occurs at a larger value of $\beta$. In Fig. 14, a phase portrait around the period-4 orbits on the $X$-axis is shown for $K = 3.3$ and (a) $\beta = 0.933$ and (b) $\beta = 1.57$, respectively. For both cases, the residue

$R^{(4)}$ is equal to $\sim 0.75$. The period-4 orbits on the $X$-axis $(X_0, P_0 = 0)$ and $(-X_0, P_0 = 0)$ are surrounded by the Poincaré-Birkhoff multifurcated period-3 orbits. In Fig. 14(a), we can recognize that here occurs the period-3 catastrophe, where the period-4 islands are squeezed into points by the period-3 orbits. On the other hand, in Fig. 14(b), we see the period-3 multifurcation around the original period-4 orbits.

Now, at the value of $\beta = 1.26$, the residue $R^{(4)}(X_0, P_0 = 0)$ becomes unity, suggesting the occurrence of the Poincaré-Birkhoff multifurcation. Figure 15 shows that two pairs of the period-2 orbits are multifurcated at $\beta = 1.26$ for $K = 3.3$. Following Greene *et al.*[8], let us examine this feature of the pair of period-2 orbits in some detail. Since the $a$-branch period-4 orbits is symmetric with respect to the origin, the points $(X_0, P_0 = 0)$ and $(-X_0, P_0 = 0)$ are regarded as the same point, and the Poincaré-Birkhoff period-4 sequence has a square root map. A study of the residue $R^{(2)}$ of the $T^2$ map gives

$$\begin{aligned} R^{(2)}(X_0, P_0 = 0) &= R^{(2)}(-X_0, P_0 = 0) \\ &= -\frac{1}{4} F'(X_0) \left[2G'(0) + 2G'(F(X_0)) + G'(0)G'(F(X_0))F'(X_0)\right] \end{aligned} \tag{59}$$

Thus, we can confirm that the residue $R^{(4)}(X_0^{(a)}, P_0 = 0)$, in Eq. (53) may be factored into

$$R^{(4)} = 4R^{(2)}[1 - R^{(2)}] \tag{60}$$

which has a maximum of 1 at $R^{(2)} = 1/2$. We show in Fig. 16 the $\beta$-dependence of the residue $R^{(2)}$, in Eq. (59) and $R^{(4)}$, in Eq. (53) for $K = 3.3$. At the stable elliptic point, the characteristic multiplier $\lambda$

$$\lambda = 1 - 2R \pm 2[R(R-1)]^{1/2} \tag{61}$$

is expressed in terms of the rotation number $\rho$, previously defined in Eq. (19) as

$$\lambda = \exp(\pm i\, 2\pi\rho)\ . \tag{62}$$

When the residue passes through the values

$$R(p/q) = \sin^2(\pi p/q) \qquad p, q\text{: coprime integers}\ , \tag{63}$$

the Poincaré-Birkhoff islands of $q$ times the original period are born. At $\beta = 0.612$, $R^{(4)} = 0$ and $R^{(2)} = 1$ so that this corresponds to $p/q = 1/2$ (period-doubling) bifurcation for the $T^2$ map. At $\beta = 0.933$, $R^{(2)} = R^{(4)} = 3/4$ and the value of $p/q$ is $1/3$ for $T^2$ and $2/3$ for $T^4$, which is the case of the period-3 catastrophe observed in Fig. 9(a). On the other hand, at $\beta = 1.57$, the value $R^{(4)}$ is $3/4$ but $R^{(2)} = 1/4$, which correspond to the $2/6$ multifurcation for $T$ and the $1/6$ multifurcation for $T^2$. Therefore, two sets of the period-3 islands turn up in Fig. 9(b) rather than the period-3 catastrophe. Lastly, at the value of $\beta = 1.26$, $R^{(4)}$ approaches unity and $R^{(2)}$ passes through $1/2$, which indicates that the $2/4$ multifurcation for $T^4$ and the $1/4$ for $T^2$ map. These 4-cycles are observed as two pairs of the period-2 orbits in Fig. 10.

# VII. Concluding Remarks

We have investigated the nonlinear dynamics of particle acceleration in the relativistic standard map and shown that the relativistic effects suppress the stochastic motion of the particles. Under the action of the coherent spectrum of electrostatic waves whose phase velocity is much larger than the speed of light, $\beta = \omega/kc \gg 1$, the particle motion becomes regular with even-numbered periodic orbits being the dominant feature over the phase space. The structure of the periodic orbits is analyzed by constructing families of space inversion and momentum reflection symmetry lines. We show that the odd-numbered periodic orbits are washed out in the stochastic sea, while the even-numbered orbits survive up to quite high periodicity. This difference in behavior is due to the fact that in the high momentum region the phase advancement for the particle motion is asymptotically constant, which is clearly shown by the family of space inversion symmetry lines becoming asymptotically parallel to

the $P$ axis in Fig. 4.

For the observed phase space structure, we were able to determine analytically the outermost KAM surface with Eq. (23), which agrees well with the numerical observation for the regime $\beta \gg 1$. For the sub-relativistic regime $\beta < 1$, we show that even though the fixed points of high momentum $P_m \approx m \approx \beta^{-1}$ are allowed to exist, the outermost KAM surface for particles with the initial momentum $P_0 = 0$ is formed as a separatrix between much lower order momentum $P_m$ fixed points, with $m \ll \beta^{-1}$.

In this connection, it is worth noting that Howard and Hohs[12] have examined the formation of an adiabatic barrier for phase space orbits in a two-parameter Hamiltonian system with a quadratically nonlinear phase advance. They showed that the nonlinear variation can give rise to a reconnection of the KAM curves and the formation of phase space vortex structures for the period-2 aligned islands. In our problem, for small $\beta$, the relativistic phase advancement could be approximated by the cubic phase advance $(P - \frac{1}{2}\beta^2 P^3)$, which may partially account for the barrier formation as observed in Figs. 2(c) and (d). Yet, it should be noticed that the derivative $G'$ of the phase transformation function $G(P)$ is positive definite in its exact relativistic expression in Eq. (10). Howard and Hohs[12] identify the critical condition for their barrier structure to occur at the point where the phase advance is stationary $(G' = 0)$. For predicting the existence of KAM barriers, our observation that the momentum inversion symmetry curves asymptotically approach to the outermost KAM surface provide a theoretical clue for determining their structure.

Turning to the super-relativistic regime $\beta > 1$, we have discovered the occurrence of the interchange of the stability of the periodic orbits around the fixed point at the origin with variations of the phase advancement parameter $\beta$. We have shown analytically by calculating the residue of the period-3 and period-4 orbits, that the stable-unstable interchange can be explained by the local linear stability properties of the orbits. Our preliminary study of the period-3 orbits for the logistic twist map examined by Howard and Hohs indicates that a

similar stability interchange can be observed for $K = 3.3$ around $\alpha \approx 0.03$. Thus, we expect that the stability interchange of the periodic orbits upon variation of the phase advancement parameter appears to be a generic features of two parameter Hamiltonian systems containing a nonlinear phase advance.

## Acknowledgments

We thank T. Kamimura and T. Hatori for their stimulating discussions, and to A.J. Lichtenberg for calling our attention to the work of Howard and Hohs. This work was supported in part by the U.S. Dept. of Energy contract #DE-FG05-80ET-53088.

## References


1. B.V. Chirikov, Phys. Rep. **52**, 265 (1979).

2. J.M. Greene, *Statistical Physics and Chaos in Fusion Plasmas,* eds. W. Horton and L.E. Reichl (John Wiley, New York, 1984) p. 3.

3. R.B. White, *ibid,* p. 209.

4. C.F.F. Karney, Phys. Fluids **22**, 2188 (1979).

5. T. Tajima and J.M. Dawson, Phys. Rev. Lett. **43**, 267 (1979).

6. C.E. Clayton, C. Joshi, C. Darrow, and D. Umstadter, Phys. Rev. Lett. **54**, 2343 (1985).

7. A.A. Chernikov, T. Tél, G. Vattay, and G.M. Zaslavsky, Phys. Rev. A **40**, 4072 (1989).

8. Y.H. Ichikawa, T. Kamimura, and T. Hatori, Physica D **29**, 247 (1987).

9. J.M. Greene, R.S. MacKay, F. Vivaldi, M.J. Feigenbaum, Physica D **3**, 468 (1981).

10. E. Pina and L.J. Lara, Physica D **26**, 369 (1987).

11. Y.H. Ichikawa, T. Kamimura, T. Hatori, and S.Y. Kim, Prog. Theor. Phys. Suppl. **98**, 1 (1989).

12. J.E. Howard and S.M. Hohs, Phys. Rev. A **29**, 418 (1984).

## Figure Captions

1. Particle orbits of the relativistic standard map for the stochastic parameter $K = 1.3$ and the relativistic parameter $\beta < 1$, a) $\beta = 0$, b) $\beta = 0.04\pi$, c) $\beta = 0.1\pi$ and d) $\beta = 0.2\pi$, respectively.

2. Particle orbits of the relativistic standard map for the stochastic parameter $K = 1.3$ and the relativistic parameter $\beta > 1$, a) $\beta = 0.4\pi$, b) $\beta = \pi$, c) $\beta = 4\pi$ and d) $\beta = 10\pi$, respectively.

3. The $\beta$-dependence of the phase space structure of the relativistic standard map with $K = 1.3$ for a) $\beta = 0$, b) $\beta = 0.2\pi$, and c) $\beta = 4\pi$, respectively.

4. Space inversion symmetry lines $\Gamma_j$ of the relativistic standard map for $K = 1.3$ and $\beta = 4\pi$.

5. Momentum inversion symmetry lines $\gamma_j$ of the relativistic standard map for $K = 1.3$ and $\beta = 4\pi$.

6. Identification of the multi-periodic island structure in terms of families of the space inversion symmetry curves $\Gamma_j$ in a), and the momentum inversion symmetry curves $\gamma_j$ in b).

7. Overall feature of interchange of the stability of multi-periodic orbits with respect to the variation of $\beta$. The real line indicates the region where the specified periodic orbit on the $X$-axis remains stable, while the broken line indicates an unstable region. This figure is for the case of $K = 2.1$.

8. Interchange of the stability of period-4 orbits between a) $\beta = 2.20$ and b) $\beta = 2.83$ at $K = 3.3$. Careful observation can identify the two sets of period-3 orbits for the case b).

9. Interchange of the stability of period-3 and period-4 orbits between a) $\beta = 2.20$ and b) $\beta = 2.51$ at $K = 6.4717$, where the fundamental fixed point at the origin bifurcates into the period-2 orbits.

10. Residue of the period-3 orbit at $K = 3.3$.

11. Residue of the period-4 orbit at $K = 3.3$.

12. Residue of the period-3 orbit at $K = 6.4717$.

13. Residue of the period-4 orbit at $K = 6.4717$.

14. Multifurcation of period-3 orbits out of the period-4 orbits at $K = 3.3$. a) period-3 catastrophe at $\beta = 0.933$ and b) two pairs of period-3 islands at $\beta = 1.57$.

15. Multifurcation of period-2 orbits out of the period-4 orbits at $K = 3.3$ and $\beta = 1.27$.

16. Residues $R^{(2)}$ and $R^{(4)}$ for the Poincaré-Birkhoff period-4 orbit on the $X$-axis at $K = 3.3$.

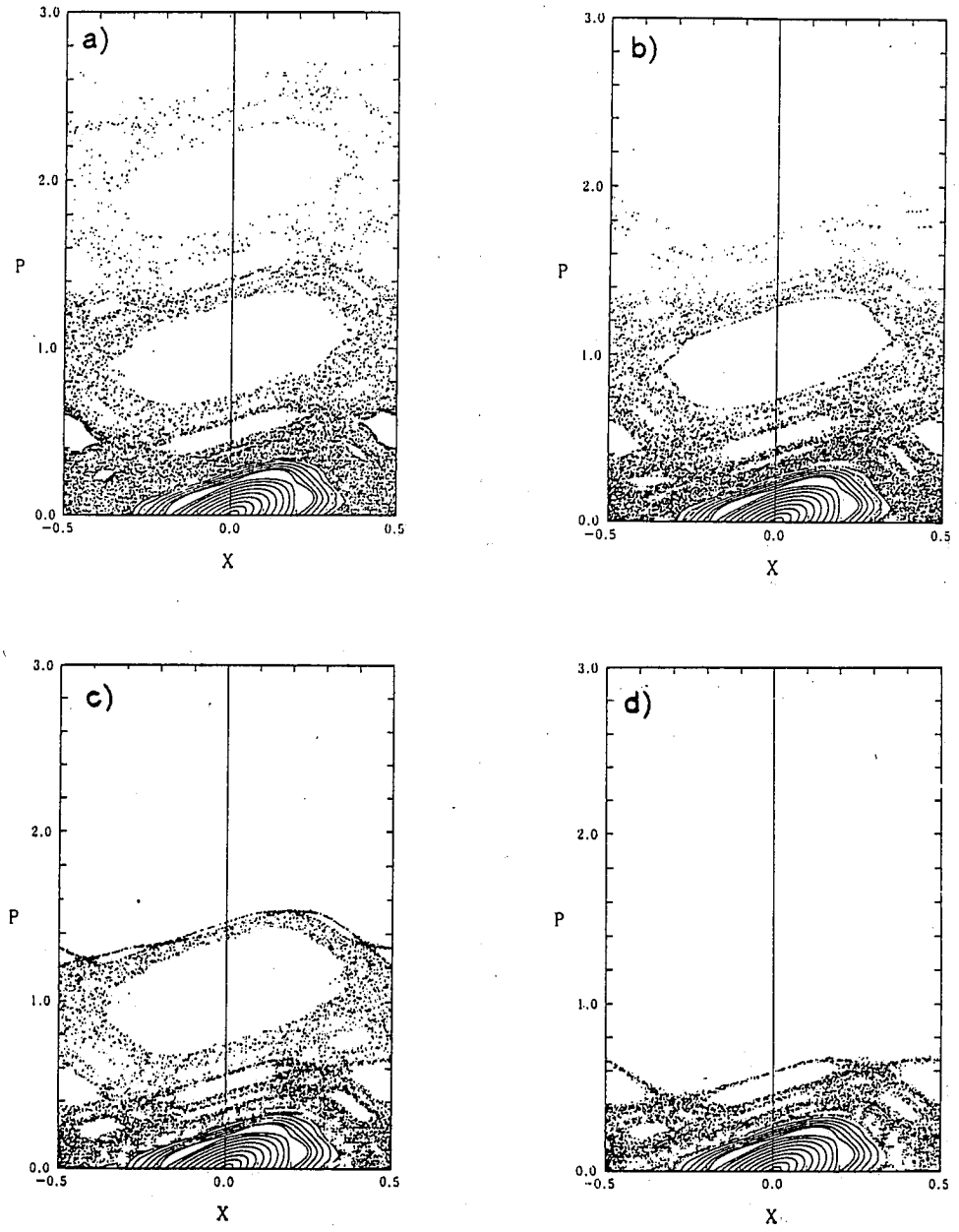


Fig. 1

a) b) c) d)

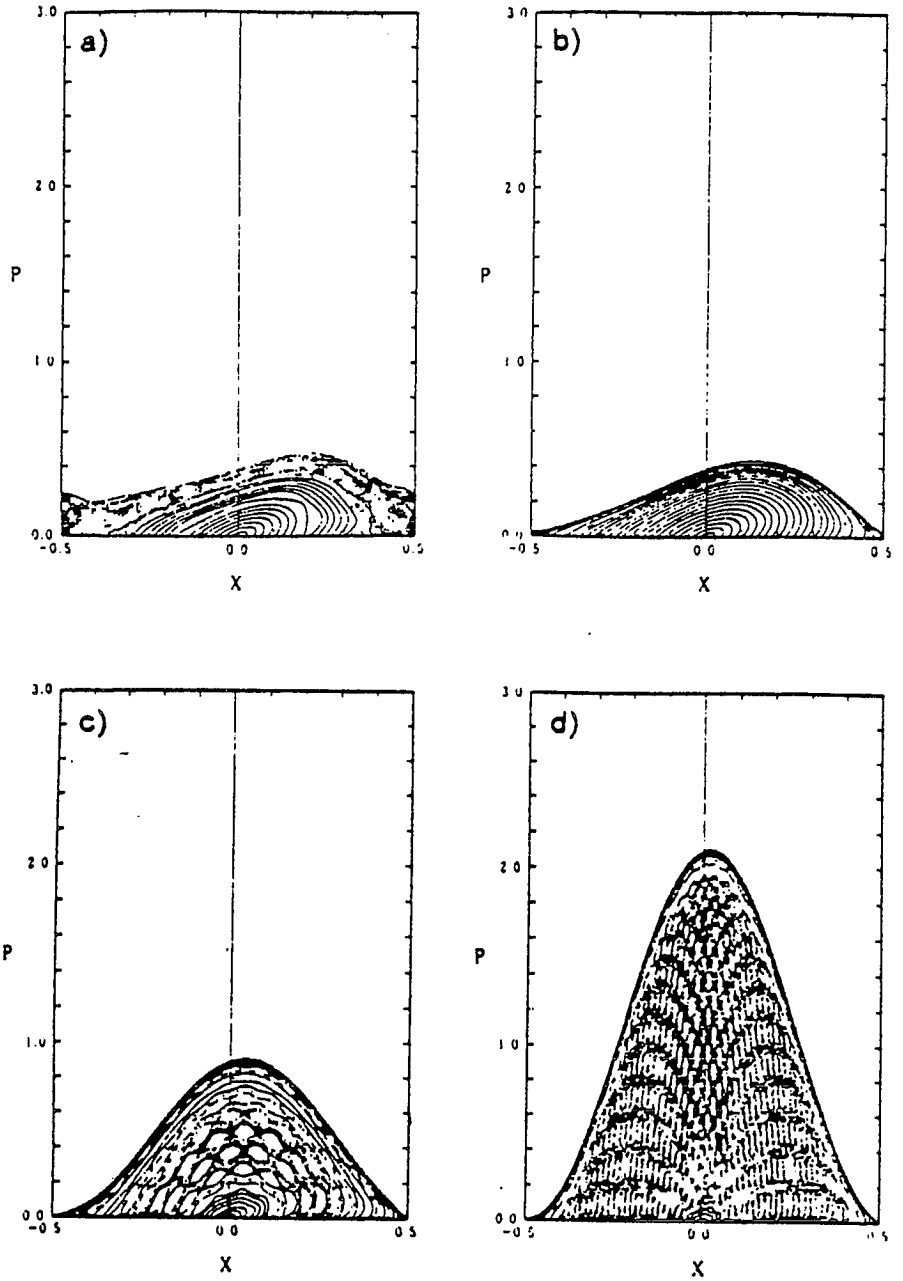


Fig. 2

a) b) c) d)

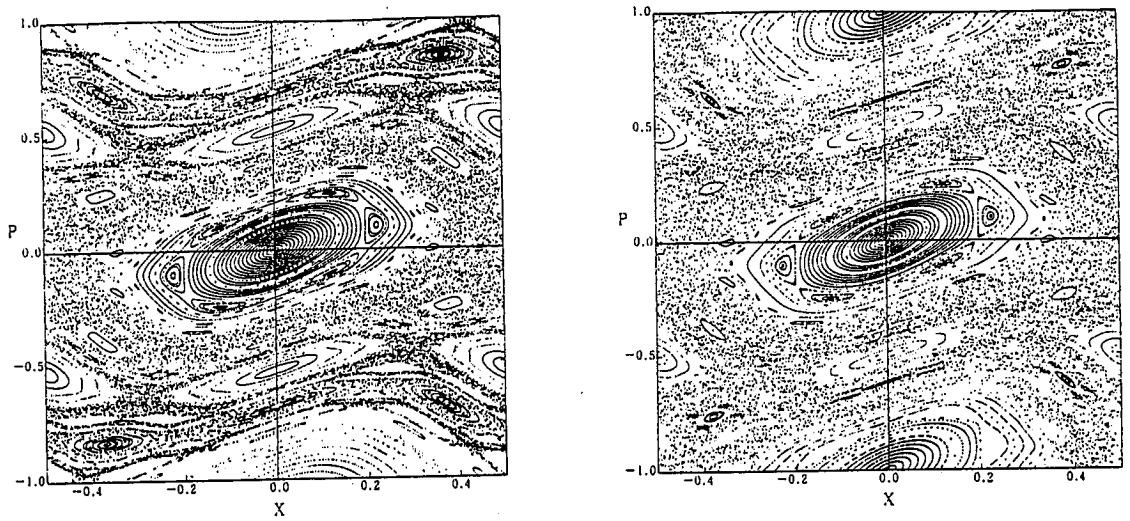


Fig. 3

a) & b)

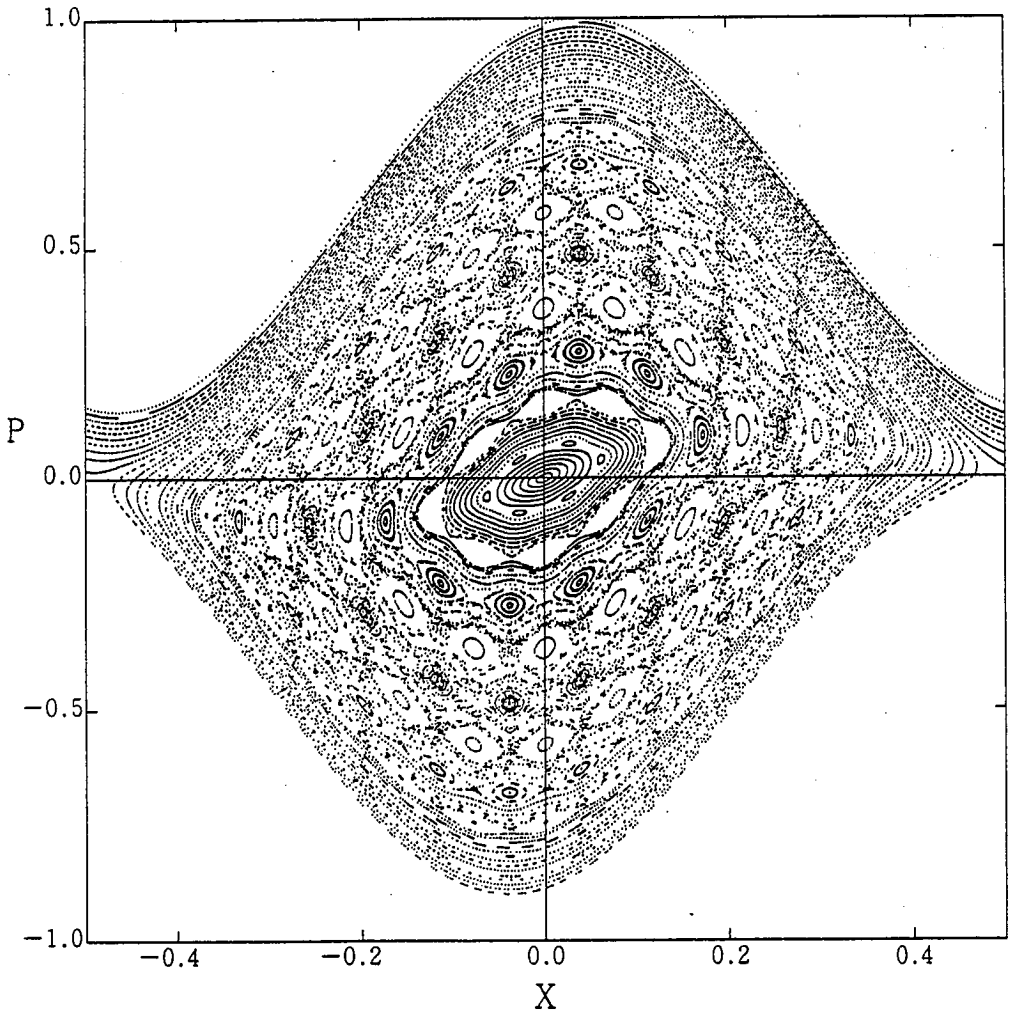


Fig. 3. c)

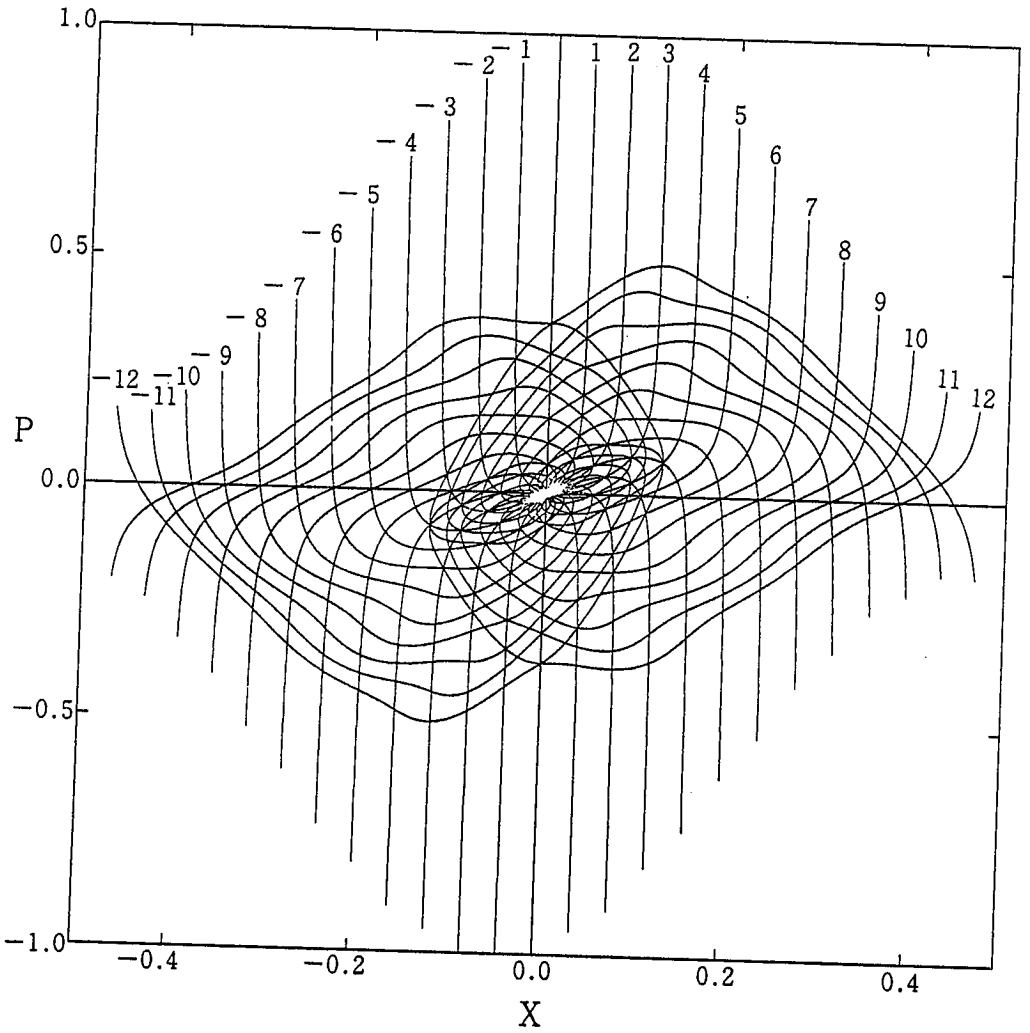
1.0
0.5
0.0
−0.5
−1.0
P
−0.4
−0.2
0.0
0.2
0.4
X
−1
−2
−3
−4
−5
−6
−7
−8
−9
−10
−11
−12
1
2
3
4
5
6
7
8
9
10
11
12

Fig. 4.

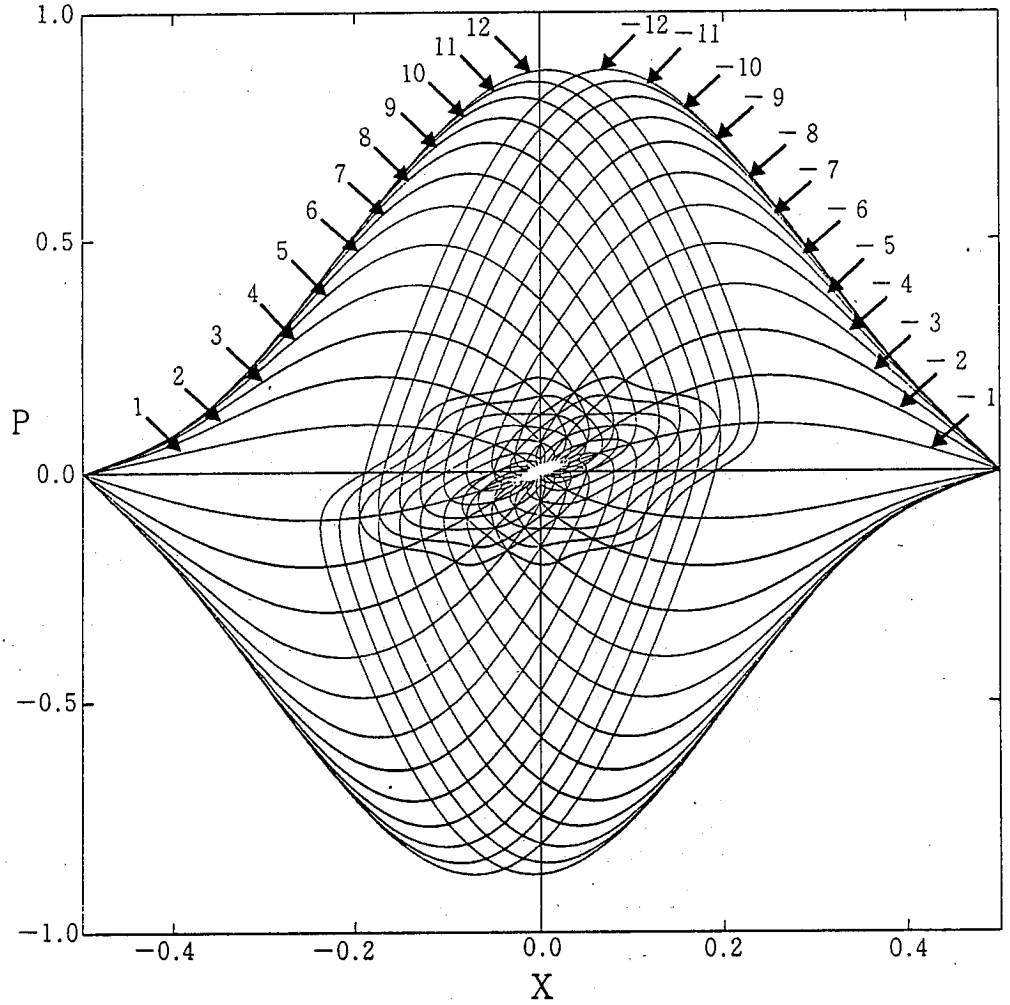
1.0
0.5
0.0
−0.5
−1.0
P
−0.4
−0.2
0.0
0.2
0.4
X
1
2
3
4
5
6
7
8
9
10
11
12
−12
−11
−10
−9
−8
−7
−6
−5
−4
−3
−2
−1

Fig. 5

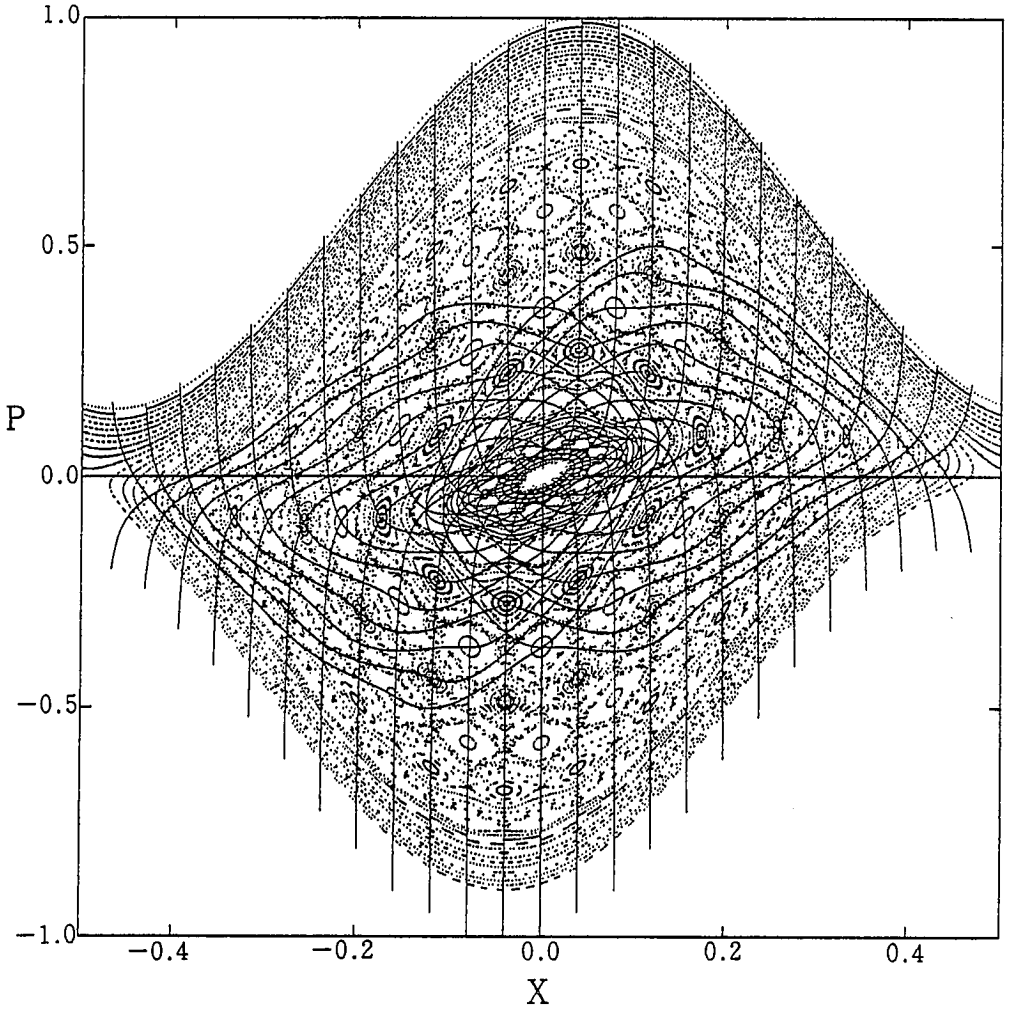


Fig. 6

a)

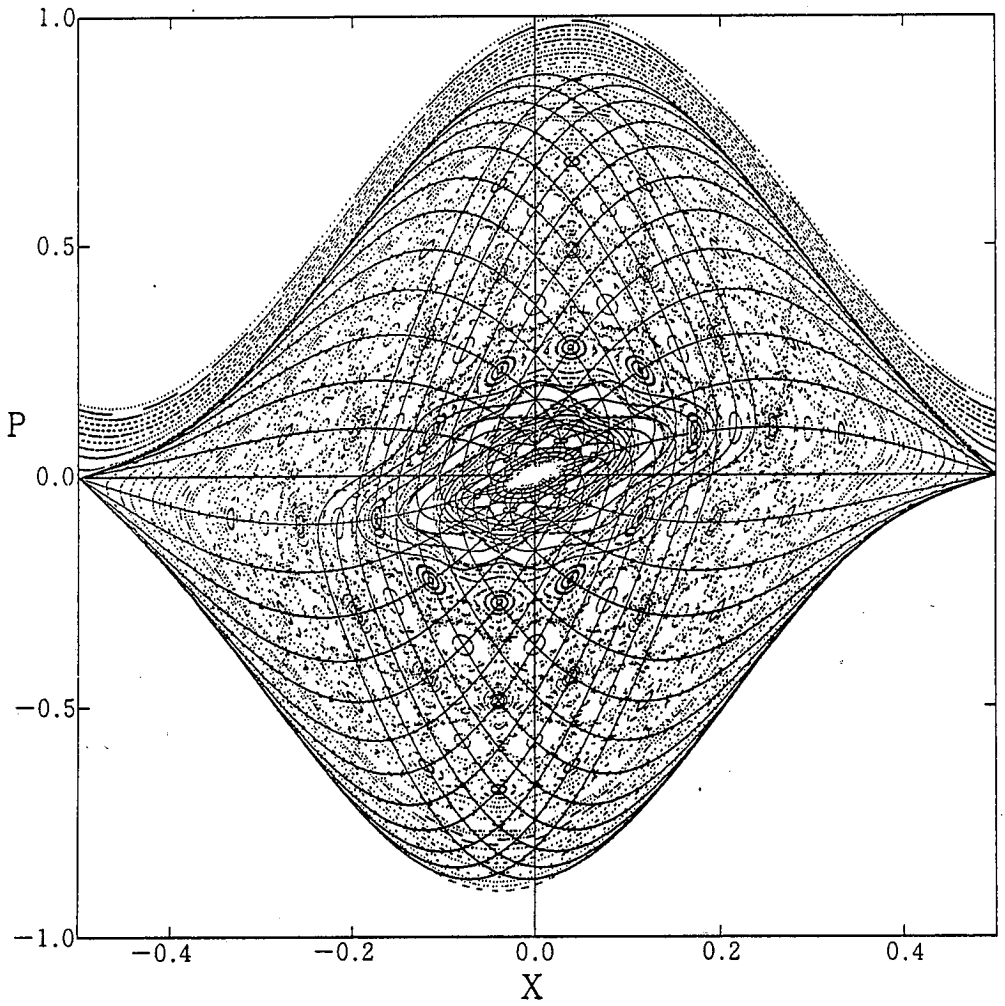


Fig. 6

e)

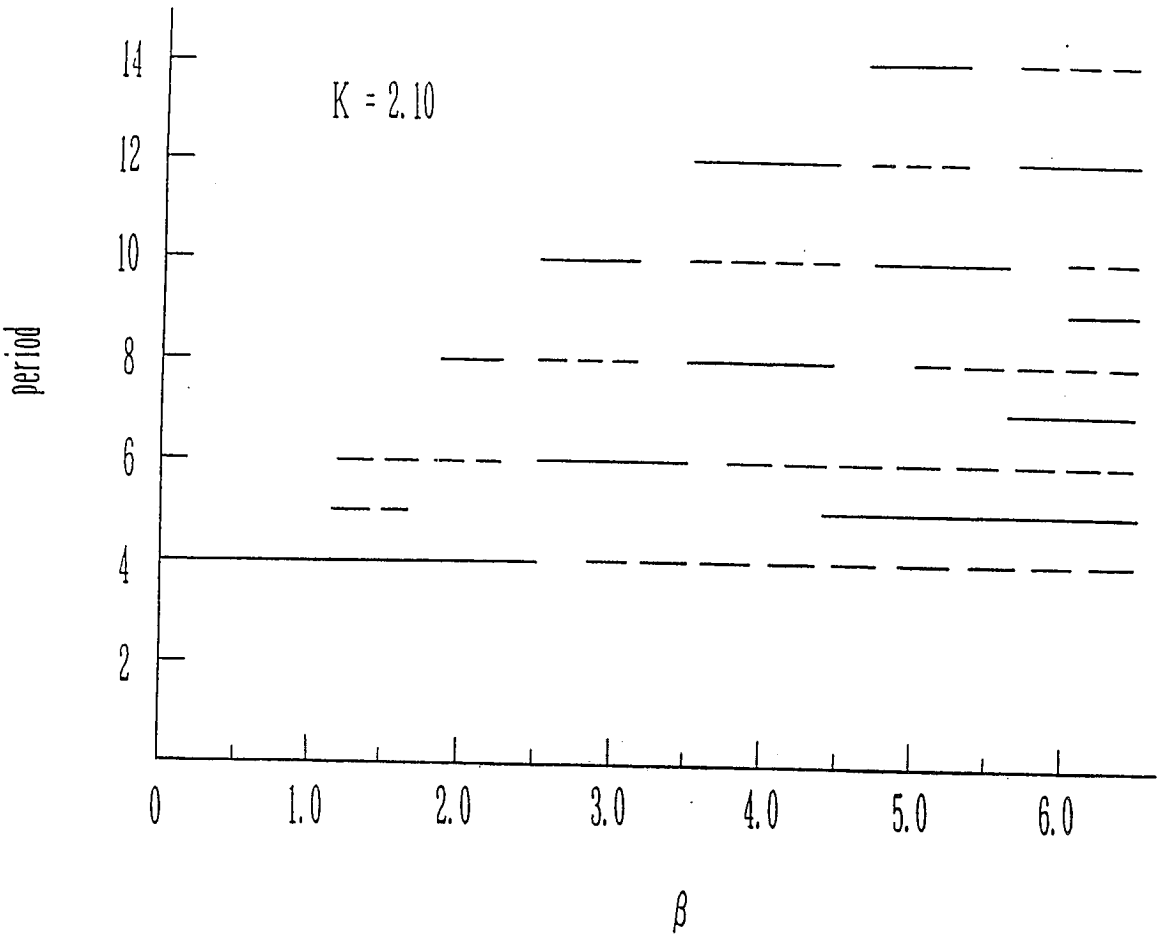


Fig. 7

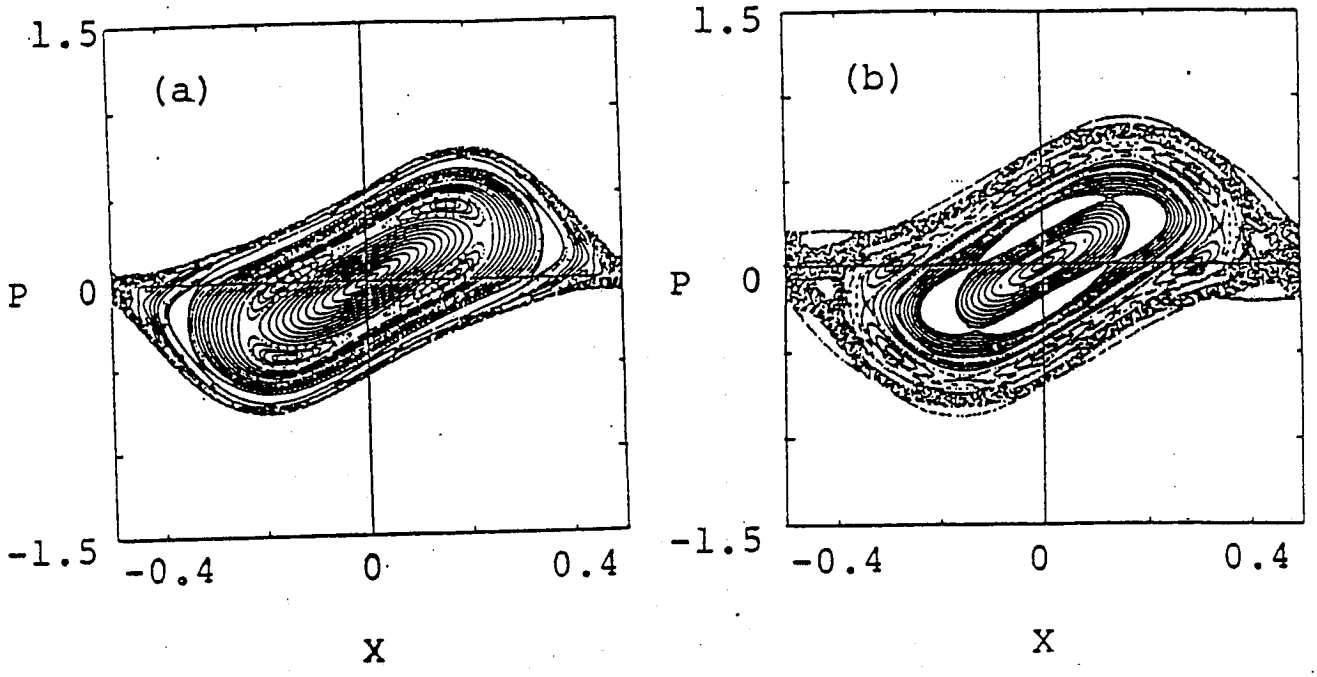


Fig. 8

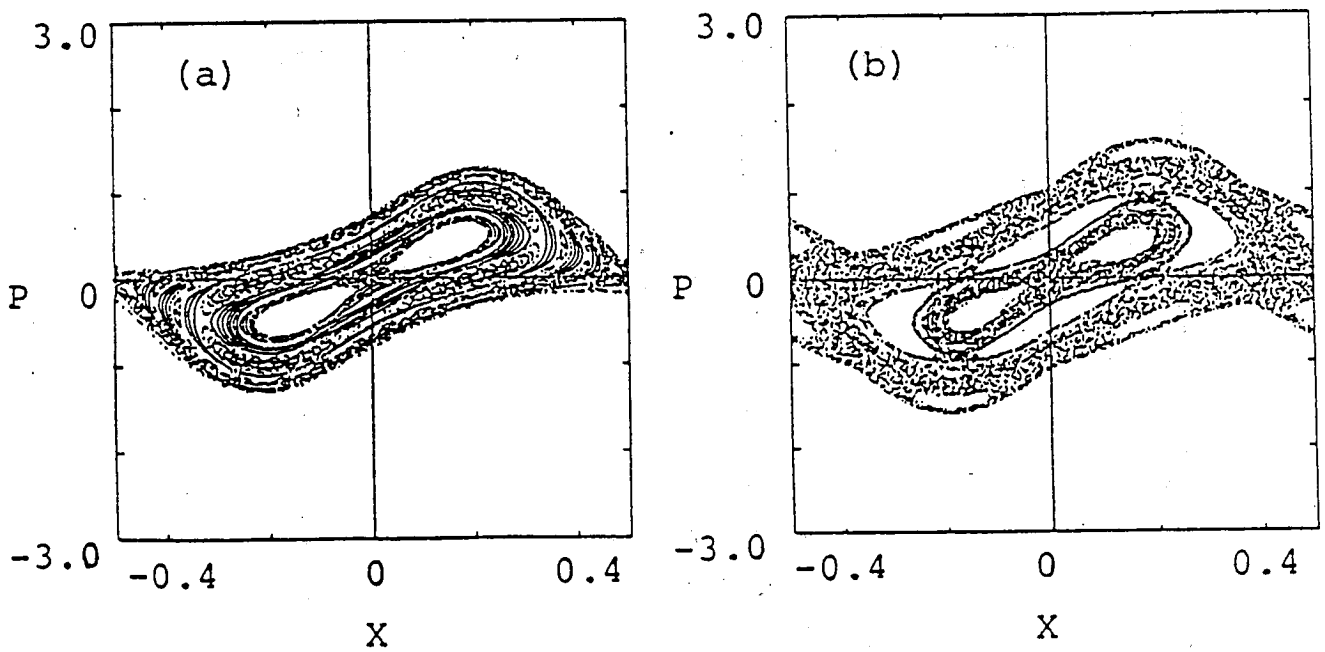


Fig. 9

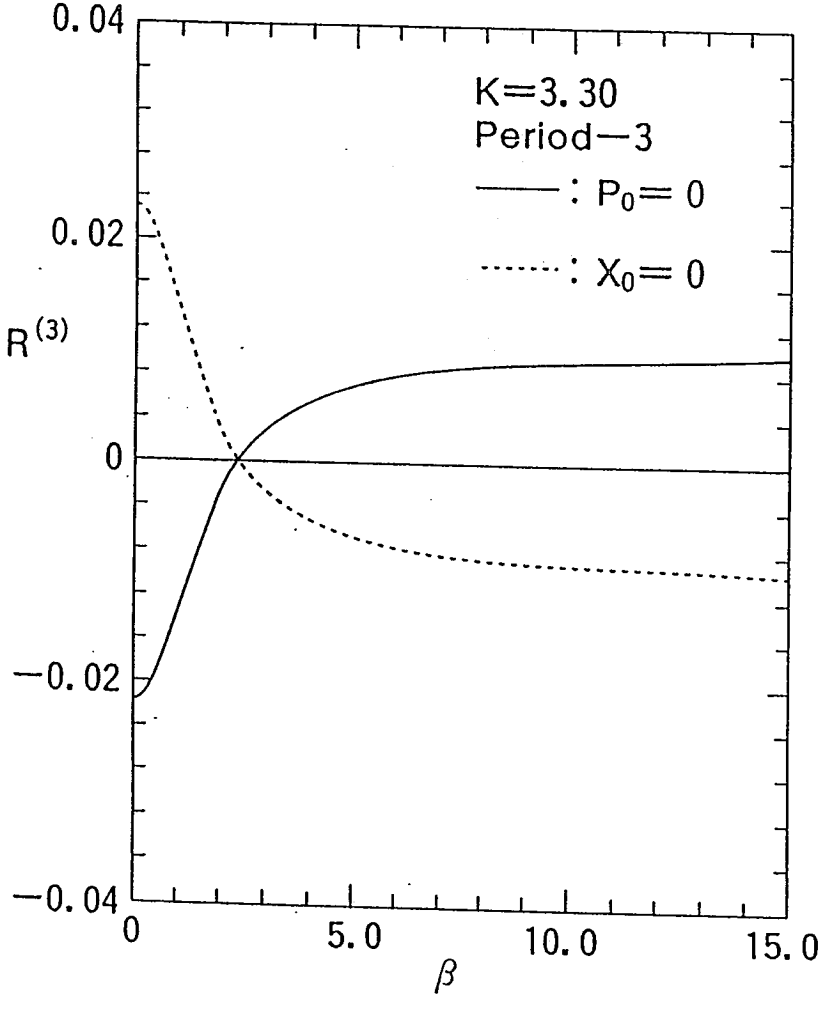
0.04
0.02
0
−0.02
−0.04
R(3)
K=3.30
Period−3
——: P0= 0
------: X0= 0
0
5.0
10.0
15.0
β

Fig. 10

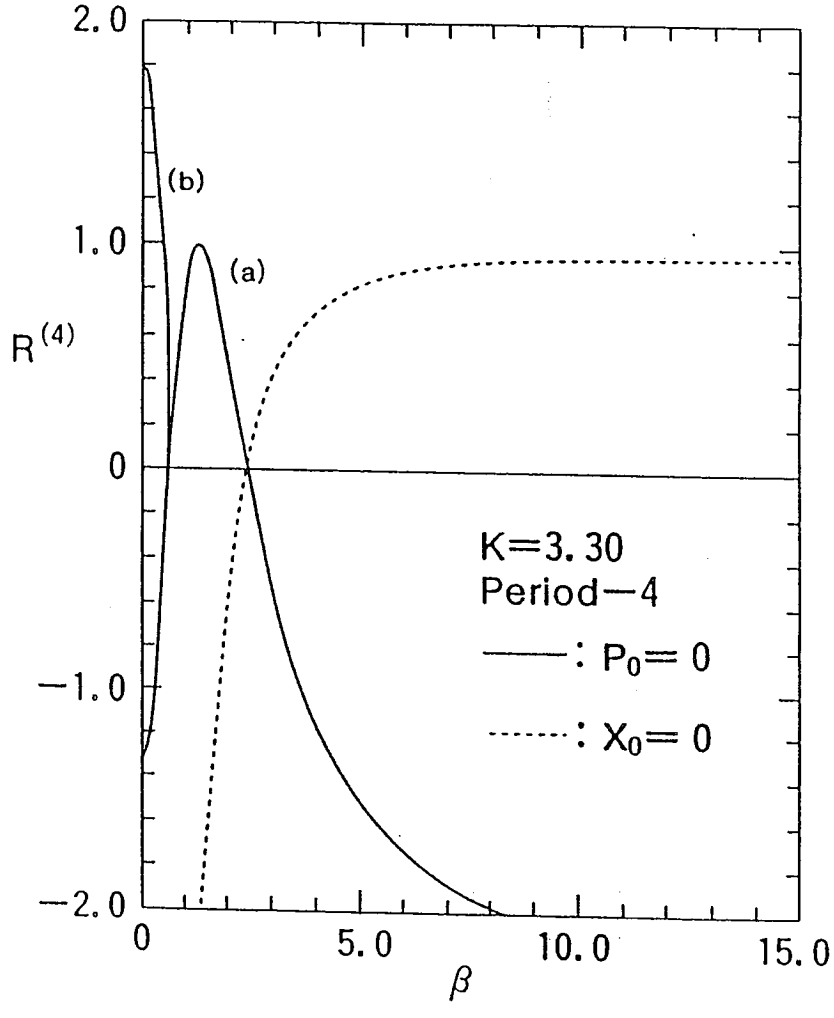
2.0
1.0
0
−1.0
−2.0
R(4)
(b)
(a)
K=3.30
Period−4
——: P0= 0
------: X0= 0
0
5.0
10.0
15.0
β

Fig. 11

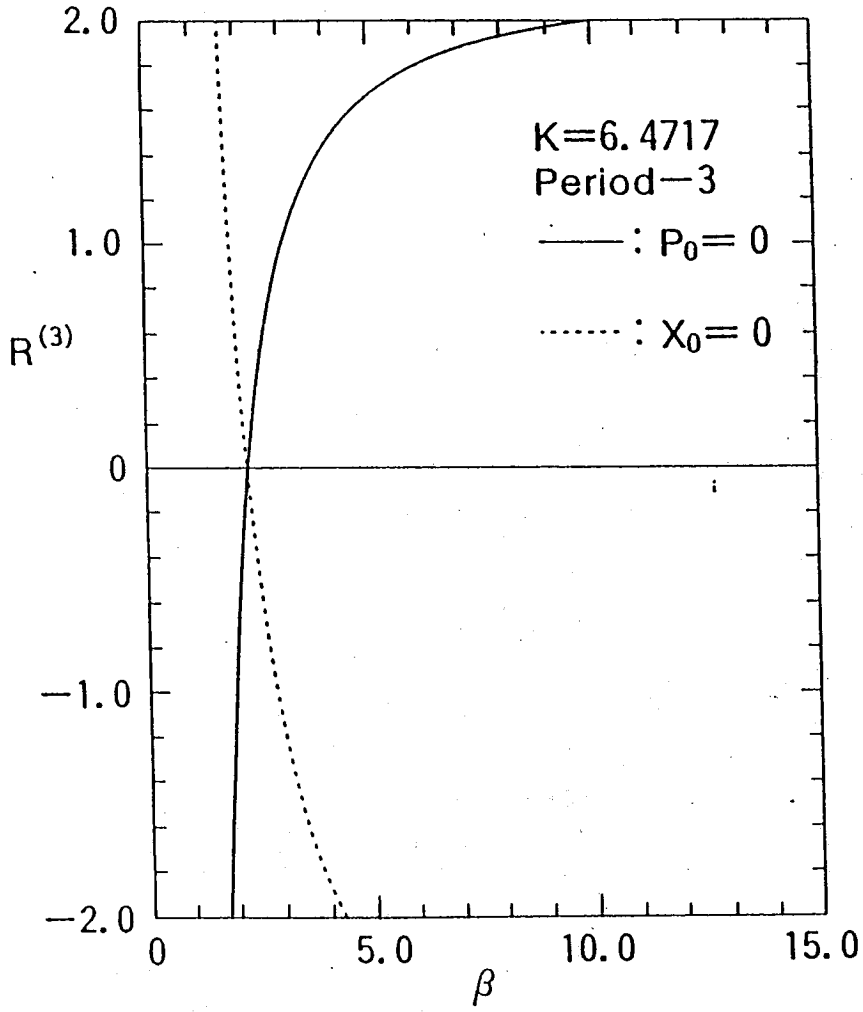
2.0
1.0
0
−1.0
−2.0
$R^{(3)}$
K=6.4717
Period−3
——: $P_0$= 0
·····: $X_0$= 0
0
5.0
10.0
15.0
β

Fig. 12

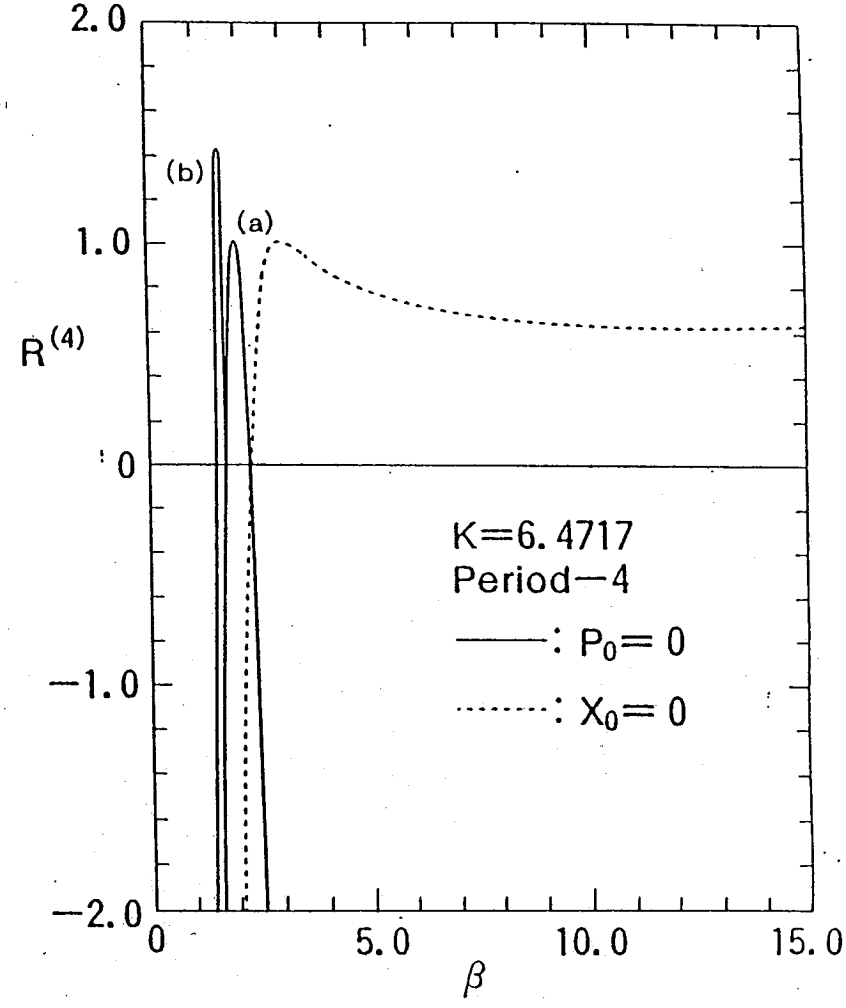
2.0
1.0
0
−1.0
−2.0
$R^{(4)}$
(b)
(a)
K=6.4717
Period−4
——: $P_0$= 0
·····: $X_0$= 0
0
5.0
10.0
15.0
β

Fig. 13

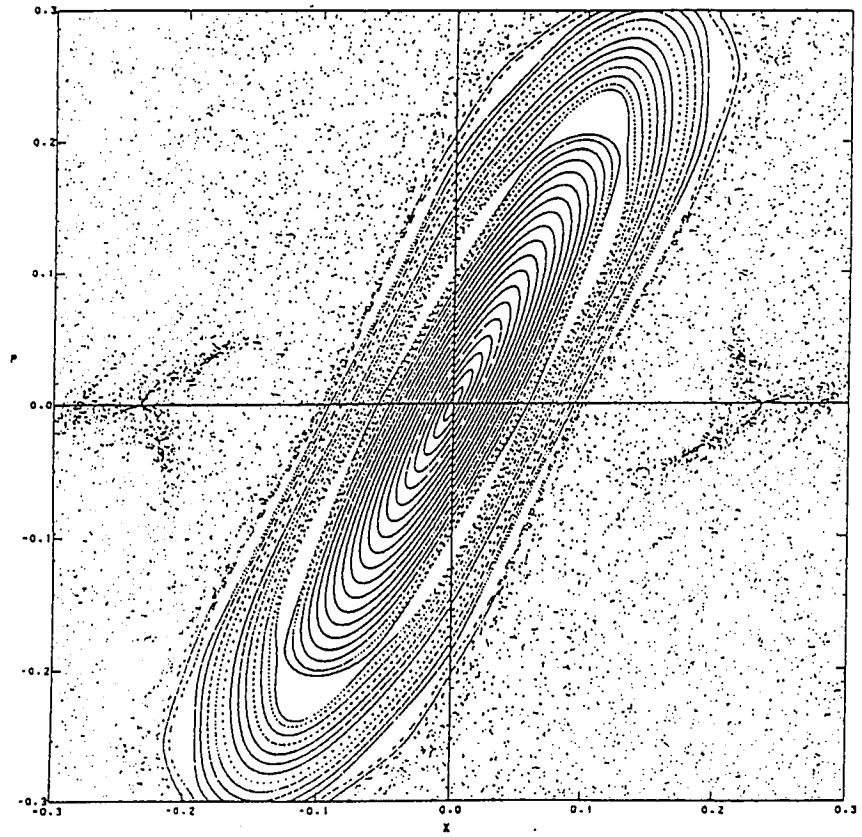
0.3
0.2
0.1
0.0
-0.1
-0.2
-0.3
P
-0.3
-0.2
-0.1
0.0
0.1
0.2
0.3
X

Fig. 14

a)

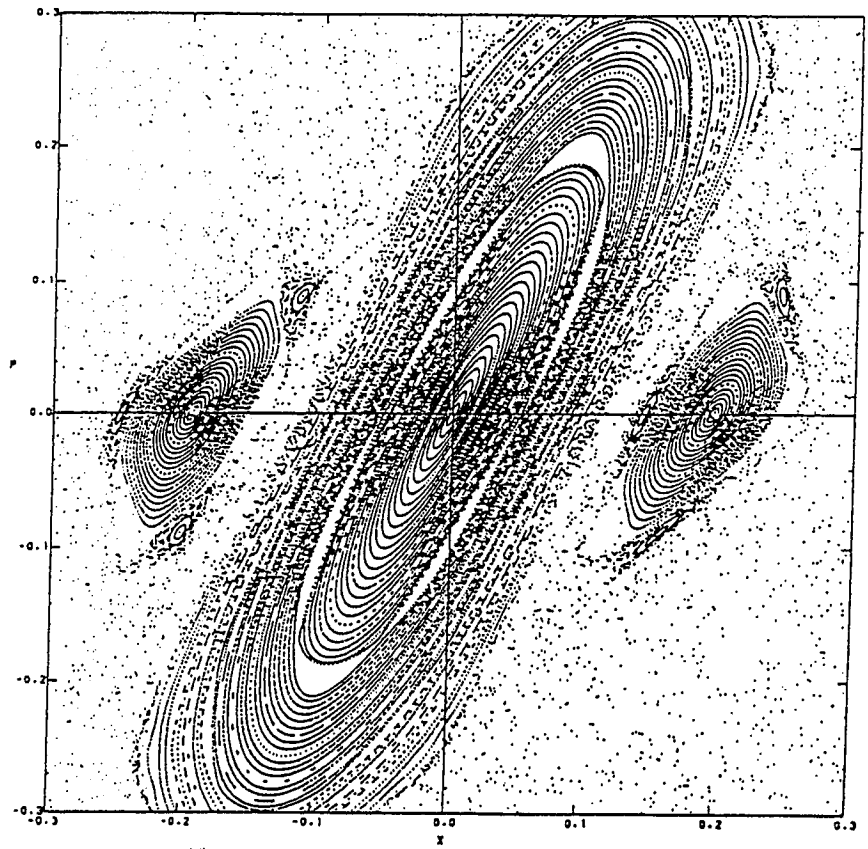
0.3
0.2
0.1
0.0
-0.1
-0.2
-0.3
P
-0.3
-0.2
-0.1
0.0
0.1
0.2
0.3
X

b)

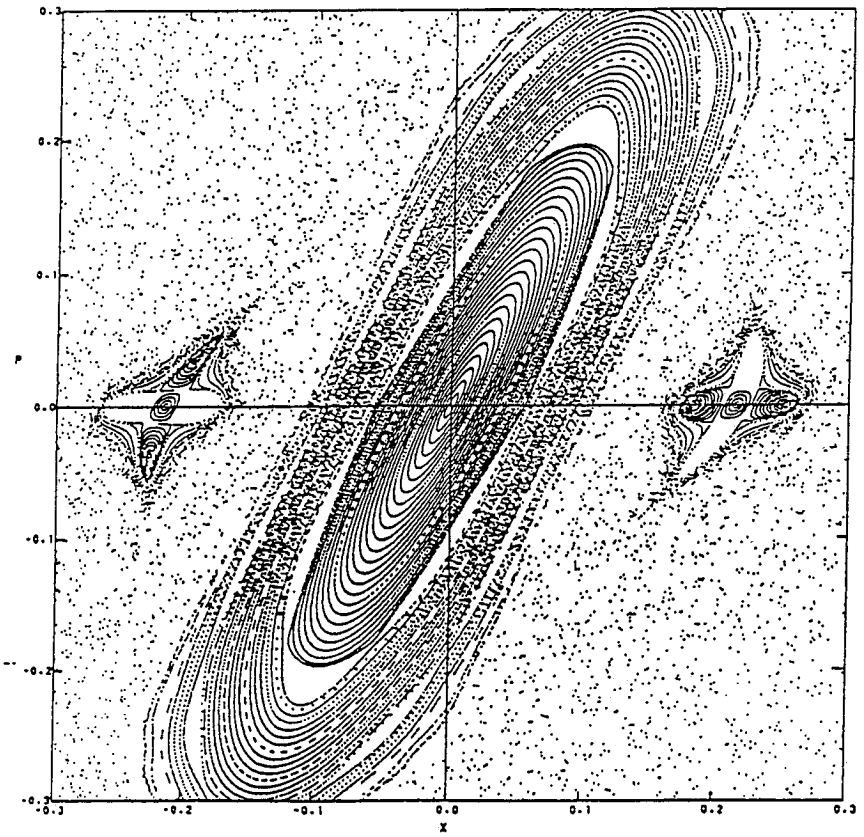


Fig. 15

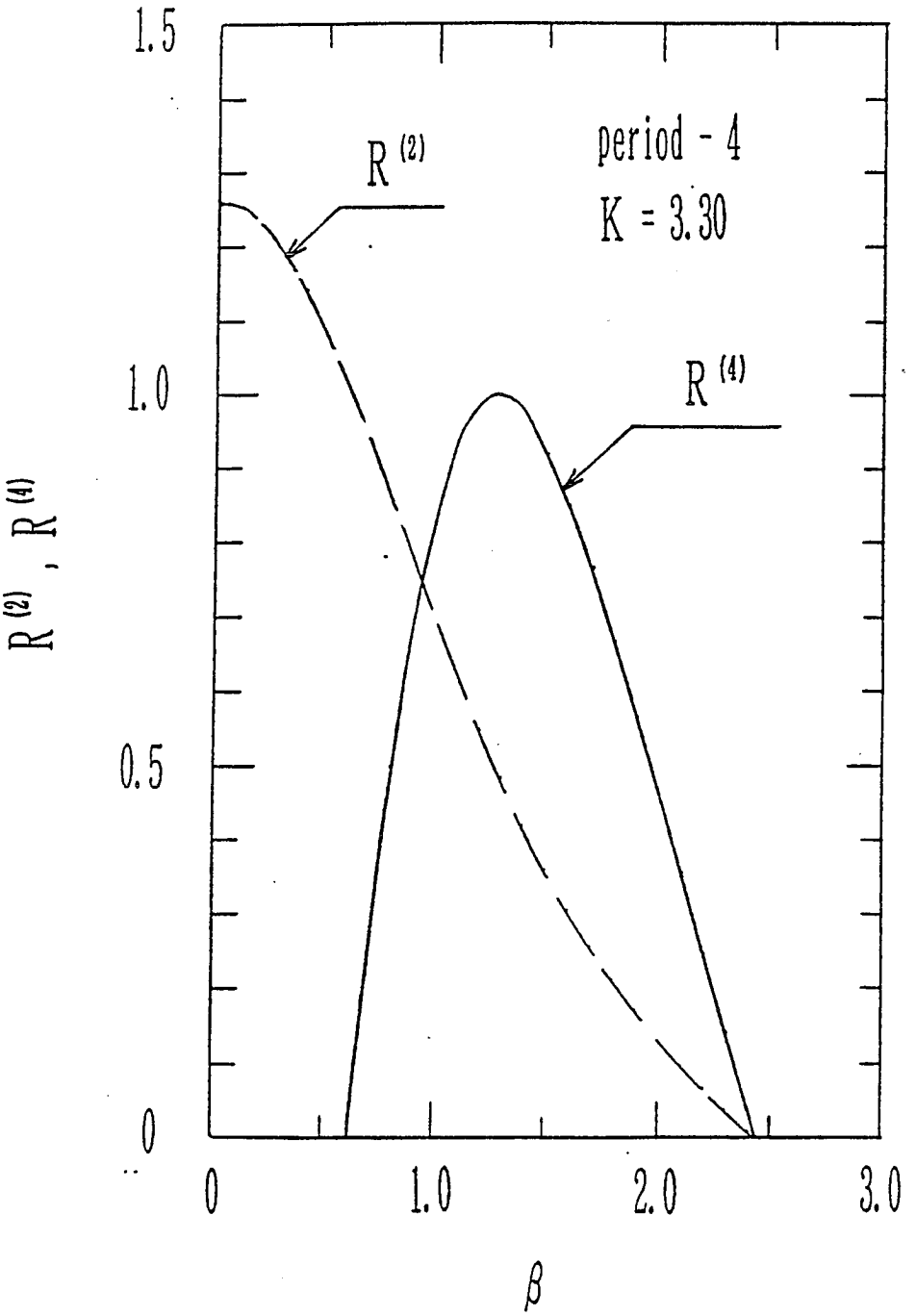


Fig. 16

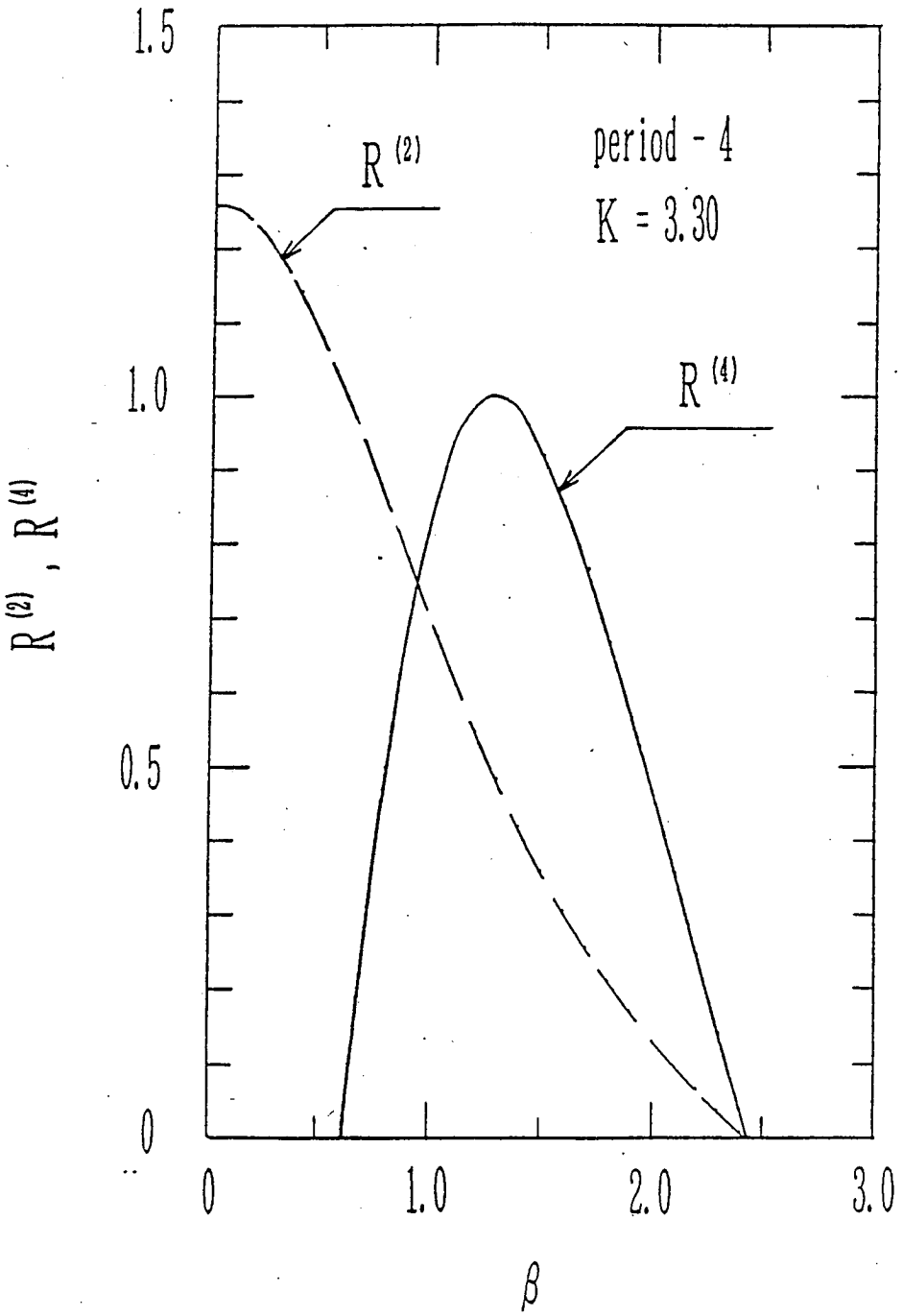


Fig. 16